- RESEARCH PAPER

International Journal of Mining and Geo-Engineering

IJMGE

IJMGE 59-4 (2025) 399-407

DOI: 10.22059/IJMGE.2025.400112.595287

Monitoring CO_2 injection in a shale gas reservoir through cross-well seismic and electromagnetic tomography

Seyed Masoud Ghiasi [a] and Maysam Abedi [b, *]

[a] *Institute of Geophysics, University of Tehran, Tehran, Iran.*

[b] *School of Mining Engineering, College of Engineering, University of Tehran, Tehran, Iran.*

Article History:

Received: 05 August 2025.

Revised: 21 September 2025.

Accepted: 01 November 2025.

ABSTRACT

Carbon dioxide (CO_2) injection, also known as geological carbon sequestration or carbon capture and storage, is a critical strategy for mitigating anthropogenic CO_2 emissions and their subsequent impact on the physical and petrophysical properties of subsurface formations. Shale gas reservoirs are receiving increased attention, with CO_2 injection emerging as a leading technology for enhancing gas recovery and achieving carbon storage. This study employs cross-well tomography, incorporating both seismic and electromagnetic (EM) methods, to monitor the CO_2 injection process within a synthetic shale gas reservoir model. The methodology utilizes time-lapse cross-well tomography data acquired before and after CO_2 injection. Seismic P-wave velocity (Vp) and electrical resistivity (ρ) serve as key physical parameters in detecting CO_2 distribution. A mixed-norm inversion technique is applied to improve the resolution and accuracy of recovered models. The results demonstrate that seismic tomography is effective in delineating changes in P-wave velocity associated with CO_2 saturation, while electromagnetic tomography captures resistivity variations indicative of CO_2 migration. Integrated seismic-EM tomography provides a comprehensive framework for monitoring CO_2 injection, enhancing the reliability of long-term carbon storage assessments.

Keywords: *CO_2 injection, Cross-well tomography, Seismic tomography, Electromagnetic tomography, Mixed-norm inversion.*

1. Introduction

Hydrocarbons serve as a vital cornerstone of global energy supply, underpinning economies and powering industries across the world. These essential compounds can be classified into two main categories: conventional and unconventional hydrocarbons, each distinguished by their unique characteristics, geological formations, and methods of extraction [1,2]. As the reserves of conventional hydrocarbons continue to depletion, there has been a marked shift in focus towards harnessing unconventional hydrocarbons. Unconventional resources are defined by their unique reservoir characteristics, which often present significant challenges in extraction due to their complex petrophysical systems. This inherent complexity necessitates the deployment of novel technology and specialized expertise, highlighting the differences in extraction methodologies required for conventional versus unconventional resources [3-5].

Unconventional hydrocarbons typically exhibit lower porosity and permeability, which necessitates the implementation of advanced stimulation techniques, including enhanced oil recovery (EOR), to achieve efficient production [2]. Shale formations, in particular, have garnered significant attention as they entrap natural gas within the source rock, preventing it from migrating to more porous reservoirs. The lack of inherent pressure within shale makes the extraction of gas and oil economically unfeasible without the application of specialized methods. Techniques such as hydraulic fracturing and fluid injection are employed to augment the flow rates from these deposits. Among the various EOR strategies, CO2 injection has emerged as a favored approach for enhancing recovery in shale reservoirs. To effectively locate these unconventional resources and monitor fluid injection processes, geophysical tools such as seismic and electromagnetic investigations have become increasingly popular [6-10].

Seismic velocity tomography is a technique used to generate high-resolution images of the Earth's subsurface by analyzing the travel times of seismic waves. Cross-well imaging is a specialized application of seismic velocity tomography that operates on a smaller scale and utilizes boreholes as both the source and receiver locations for seismic waves. This method is primarily employed to image localized areas, typically at the reservoir scale, covering distances ranging from a few hundred meters to a few kilometers. Cross-well tomography predominantly focuses on P-waves (compressional waves), as they are generally the first arrivals and can be identified with higher accuracy [11]. For several decades, cross-well seismic tomography has been widely used to produce high-resolution images of subsurface structures across various applications [12-17]. Furthermore, electromagnetic exploration is a well-established geophysical method aimed at analyzing various physical properties of subsurface structures [18-21]. Cross-well electromagnetic tomography is a specialized geophysical exploration technique that applies the principles of electromagnetism to investigate subsurface characteristics. This method involves the transmission and reception of electromagnetic waves to map underground features, particularly variations in electrical conductivity between two wells [22-27].

Seismic velocity and electrical conductivity are highly effective indicators of key reservoir properties such as porosity, saturation, temperature, and anisotropy. As a result, these methods are the primary choice for characterizing subsurface reservoirs. Integrating both seismic and electromagnetic (EM) tomography techniques enables the

* Corresponding author. *E-mail address:* maysamabedi@ut.ac.ir (M. Abedi).

acquisition of more precise results and interpretations related to the physical properties of subsurface structures [22]. While seismic methods are relatively well-established and provide valuable information on reservoir geometry and geological distributions, electrical conductivity exhibits a more direct correlation with reservoir fluid complexities. This is because factors such as porosity, pore fluid conductivity, saturation, and temperature significantly influence conductivity [22]. Consequently, despite the increased cost of surveying, the combined use of EM tomography alongside seismic tomography has become indispensable for comprehensive reservoir characterization [28-31].

One of the well-known applications of cross-well seismic-EM data acquisition is monitoring the impact of CO_2 injection on the variation of physical properties within geological structures. Capturing and injecting CO_2 produced by industrial facilities, power plants, and other sources offers significant benefits, ranging from addressing environmental concerns—such as mitigating global warming and reducing atmospheric contamination—to enhancing reservoir engineering processes. In particular, CO_2 injection can improve oil recovery by increasing reservoir pressure through CO_2 pumping [32-37].

In this study, we utilized seismic and electromagnetic (EM) tomographic data to characterize the physical properties of subsurface structures confined between two wells (assuming open hole or non-metallic casing). One well contains transmitters (sources), while the other houses receivers. The distance between the two wells is 1 km, and their depths extend to 2 km. A layered geological model was considered between the two wells, consisting of four distinct layers with a gas shale reservoir positioned approximately in the middle of the model. Figure 1 presents a schematic representation of the geological structures and the CO_2 injection process. As illustrated in the schematic, the CO_2 injection process is conducted using four boreholes (in cases involving production).

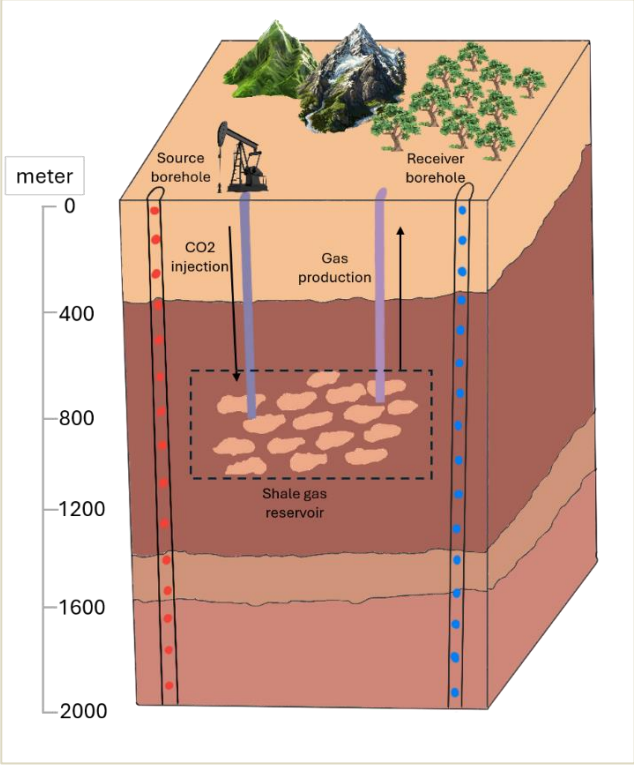

Fig. 1 A schematic map of CO2 injection in shale gas reservoir.

Since CO_2 injection alters the physical properties of the targeted structure—for instance, the presence of gas significantly reduces the velocity of compressional (P) waves, even at relatively low gas concentrations—it is crucial to monitor these changes. Additionally, CO_2 injection increases the electrical resistivity of the structure. To analyze these effects, we designed a controlled scenario before and after CO_2 injection using a realistic synthetic model. This approach allowed us to accurately recover variations in P-wave velocity and electrical resistivity resulting from changes in the physical properties of the subsurface structure.

2. .Methodology

2.1. Forward modeling of seismic and electromagnetic tomography

Seismic tomography is an inversion-based technique used to develop Earth velocity models that illustrate the influence of rock physical properties on seismic wave propagation. Generally, seismic tomography is applied in two modes: reflection and transmission. Transmission tomography involves the propagation of seismic waves through the Earth without reflection. This approach typically employs two boreholes—one containing the source or transmitter equipment and the other housing the receiver equipment.

The process of cross-well seismic tomography consists of three key steps. First, the actual travel time at the receiver positions is determined for a given source-receiver geometry. Second, ray-tracing modeling is conducted to simulate energy travel paths. Third, the travel time equations are solved to reconstruct the velocity model. Forward modeling in seismic tomography numerically calculates seismic travel times between a source and a receiver for a predefined velocity model, mapping the actual ray travel path within the given model.

According to [38], travel-time tomography corresponds to the first arrival recorded at each receiver point. Ray theory assumes that seismic waves propagate along discrete paths (rays) that adhere to Snell's law at velocity boundaries. Consequently, for a given ray path (assuming a linear trajectory), the total travel time T is obtained as follows:

$$T = \int_{x_1}^{x_2} \frac{dx}{v} \qquad (1) \qquad (1)$$

In this approach, the model space is discretized into a grid, where x_1 and x_2 represent the source and receiver locations, respectively. The algorithm seeks to determine the velocity model that adheres to Fermat's principle, ensuring that the ray path follows the trajectory with the minimum travel time.

In uniform mediums, the physics of first arrivals of p-wave or EM waves is formulated by the equation $\frac{\partial^v \varphi}{\partial t^v} = \gamma \Delta \varphi + S$. Where v can be 1 and 2 for diffusion and waves, respectively. For EM scenario, the equation can be written as [39]:

$$\frac{\partial H}{\partial t} = D\Delta H + M_0 \delta(t)\delta(\boldsymbol{X}) \qquad (2)$$

Where H is a magnetic field, M_0 is the source strength and δ is Dirac's function. The diffusivity is $D = 1/\mu\sigma$ where μ is the magnetic permeability and σ the electrical conductivity. According to the solution of eq. 2 (Green's function) [28, 29, 39-41], the travel time tomography in 2D space would be as follows:

$$\sqrt{t_p} = \frac{1}{2}\int_{x_1}^{x_2} \frac{dx}{\sqrt{D}}. \qquad (3)$$

2.2. Mixed-norm inversion

The Tikhonov L_2 inversion provides an optimization method which recovers models that are regularized to avoid overfitting. Accordingly, the objective function encompasses two terms, data misfit ϕ_d and regularization term ϕ_m. These terms can be weighted by factor λ as a trade-off parameter as follows [42]:

$$\phi = \phi_d + \beta\phi_m. \qquad (4)$$

The data misfit term corresponds to measuring how well the predicted and observed data are fitted and formulated as $\phi_d = \|W_d(d^{pred} - d^{obs})\|_2^2$ where W_d is the data weighting matrix. The regularization term which controls smallness and smoothness of the model can be expressed as $\phi_m = \alpha_s\|W_s m\|_2^2 + \sum_{i=x,y,z}\alpha_i\|W_i m\|_2^2$ where

α_s *and* α_i are multiplier weights for smallness and smoothness terms (the relative amplitudes of the terms inside ϕ_m). Those controls how much penalization is applied to amplitude versus gradients [43,44].

In this study we utilized mixed L_p norm inversion techniques introduced by [45] to provide a balanced choice between sparsity and smoothness in the recovered model. The mentioned algorithm defines the regularization term in the inversion as follows:

$$\phi_m^{pq} = \alpha_s \|W_s m\|^p + \sum_{i=x,y,z} \alpha_i \|W_i m\|^q \quad (5)$$

where $p \in [0,2]$ which is used for the smallness term and $q \in [0,2]$ is used for smoothness of the model. Other optimization parameters are maximum outer iterations (Newton/GN iterations), bound constraints on model parameters (physical bounds, e.g. positive velocity or slowness), maximum line search iterations, maximum inner conjugate gradient iterations, and CG tolerance (stopping tolerance for inner solves). According to the expression, in mixed L_p norm inversion, the regularization term applies distinct L_p norms to the smallness and smoothness components of the model structure, informed by our prior knowledge.

3. Shale gas reservoir simulation

As discussed, CO_2 injection offers various benefits, including reducing greenhouse gas emissions into the atmosphere and enhancing oil recovery at production sites. To analyze these effects, we synthetically generated a model with predefined physical properties, specifically P-wave velocity and electrical resistivity, under two distinct scenarios: the first representing conditions before CO_2 injection and the second reflecting changes after the injection process.

For this study, we assumed that the area between the boreholes consists of a layered geological structure. The first layer, with a thickness of 0.3 km, represents a sedimentary formation (such as shale or marl) with a P-wave velocity of 2,100 m/s and an electrical resistivity of 5 Ωm. The second layer, measuring 1 km in thickness, is modeled as a carbonate formation (e.g., limestone or dolomite) with a P-wave velocity of 3,100 m/s and an electrical resistivity of 100 Ωm. The third layer, a shale formation, has a thickness of 0.2 km, a resistivity of 10 Ωm, and a P-wave velocity of 2,200 m/s. The final layer, a 0.5 km-thick limestone formation, is characterized by an electrical resistivity of 150 Ωm and a P-wave velocity of 3,500 m/s.

According to our scenario, none of these primary layers are directly affected by the CO_2 injection process. However, within the second layer, we incorporated a synthetic shale gas reservoir with a thickness of 0.25 km and a width of 0.5 km, which is subject to CO_2 injection and experiences alterations in its physical properties. Before injection, the reservoir was assumed to have a P-wave velocity of 2,000 m/s and an electrical resistivity of 20 Ωm. Given that the presence of CO_2 leads to a reduction in P-wave velocity and an increase in electrical resistivity, we adjusted these values to 1,700 m/s and 40 Ωm, respectively, after injection. In our model design, the left borehole serves as the location for transmitter points, while the right borehole is designated for receiver points. The total number of sources and receivers is set to 45 each, evenly spaced at constant intervals. Based on this defined experimental setup, we aim to capture and monitor the variations in physical properties throughout the CO_2 injection process.

Figures 2a and 2b illustrate the tomography grid, where the models are discretized into X*Z squared cells, each with 20 m sides, for both the P-wave and electrical resistivity true models. In these figures, the red dots represent the source points, while the black dots indicate the receiver points. As shown, the sources and receivers are spaced uniformly at intervals of 0.1 km. Figures 2c and 2d display the results of the tomographic inversion of the true models before CO_2 injection, showing the P-wave velocity and resistivity distributions, respectively. Since we are working with a layered model, the regularization parameters are set as $L_{p=0.01}$ and $L_{qx,y=0.01}$ to achieve relatively sharp inverse models. As demonstrated, the inversion results for both the seismic and electromagnetic (EM) cases have successfully recovered accurate models, accurately capturing the layering, the position of the reservoir, and the associated values.

Figure 3 shows the first arrival times of cross-well tomography, obtained through forward modeling of P-wave velocity (3a) and electromagnetic (EM) wave velocity (3c). Each colored line corresponds to one of the source points, while the horizontal axis represents the position of each receiver. To better simulate a realistic scenario, we introduced 2% noise to the data. As a result, fluctuations in the first arrival times are evident, reflecting the impact of this added noise.

Figure 4 illustrates the scenario following CO_2 injection. In the center of the reservoir, variations in physical properties are present, which are intended to be captured (Figures 4a and 4b). Based on the inversion results post-injection, it is clear that the inversion algorithm has successfully recovered the discrepancies in both P-wave velocity and electrical resistivity, accurately reflecting the changes caused by the CO_2 injection.

Figure 5 presents the first arrival times for both seismic and electromagnetic (EM) data after CO_2 injection. As shown, the first arrival diagrams have undergone slight changes, corresponding to the variations in physical properties observed in both synthetic models due to the CO_2 injection. Experience from field-scale CO_2 storage projects supports the viability of our workflow. At the Sleipner site (North Sea, Norway), time-lapse seismic surveys effectively imaged the CO_2 plume migration within the Utsira Formation, demonstrating robust seismic monitoring under real-world conditions [36]. Similarly, at the Nagaoka pilot site in Japan, cross-well seismic tomography and repeated well-logging provided high-resolution tracking of CO_2 distribution and post-injection behavior [37]. These observations suggest that applying our integrated seismic–EM workflow in such settings could yield enhanced spatial resolution and confidence in monitoring real field deployments.

4. Discussion

Typically, the prediction of changes in seismic and electromagnetic (EM) responses of a structure is based on the physical properties of the injected zone, such as the acoustic and electrical properties of the surrounding reservoir. For instance, CO_2 is a highly compressible gas, and in zones with a weak rock matrix, the compressional velocity is particularly sensitive to the compressibility of the fluid. As a result, the presence of gas can lead to a reduction in P-wave velocity. In contrast, CO_2 is generally less conductive than water. When CO_2 is injected into a reservoir, it can displace saline water, which typically has higher conductivity due to the dissolved ions. Consequently, this displacement may result in an increase in the resistivity at the injection site.

In our study, we specifically modeled the changes induced by CO_2 injection within the target zone, which is situated in the second layer of our four-layered geological structure. The primary effect of the injection process was a reduction in P-wave velocity by 300 m/s and an increase in electrical resistivity by 20 Ω·m. These alterations were incorporated into our true models to assess the detectability of CO_2-induced changes.

Our assumed ~300 m/s Vp reduction and ~20 Ω·m resistivity increase are consistent with controlled laboratory core-flood experiments, which report several-percent to >10% decreases in P-wave velocity during supercritical CO_2 substitution [47,48,52,53]. Similarly, laboratory rock-physics measurements show monotonic increases in resistivity with CO_2 saturation [54], while field-scale monitoring at the Ketzin site documented order-unity (≈200%) resistivity growth in the injection zone [46,49,50,51]. These findings confirm that the magnitude of physical property changes assumed in our synthetic scenario lies within the range observed in both laboratory and field studies. Higher noise increases model uncertainty and weakens data sensitivity so that larger datum standard deviations down-weight the misfit so the regularizer dominates, reducing spatial resolution and making small or low-contrast anomalies harder to detect. Sparse norms (small p, small q) can sharpen boundaries and improve localization when signal-to-noise is adequate, but they are more fragile under high noise—aggressive sparsity can amplify noise into spurious isolated features while very strong regularization (large β) will instead smear true anomalies.

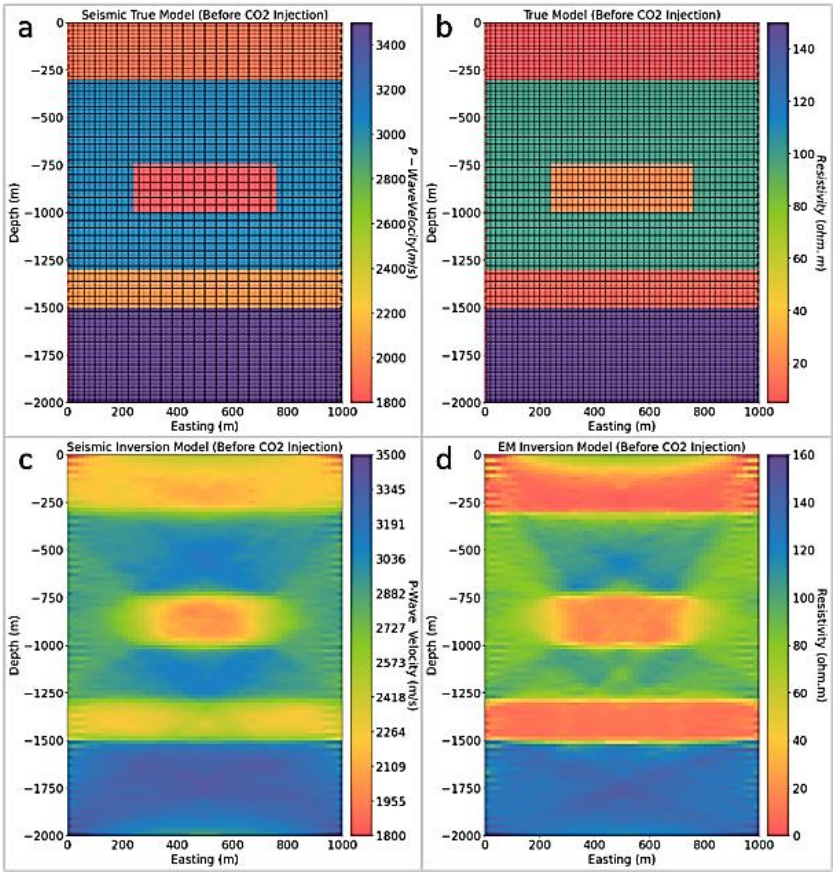

Fig.2 Geophysical simulation of a synthetic multi-layered shale gas reservoir prior to CO2 injection, focusing on two physical properties: (a) the P-wave velocity model, and (b) the electrical resistivity model. The mixed-norm inversion technique was applied to cross-well tomography data, resulting in (c) the P-wave velocity model and (d) the electrical resistivity model.

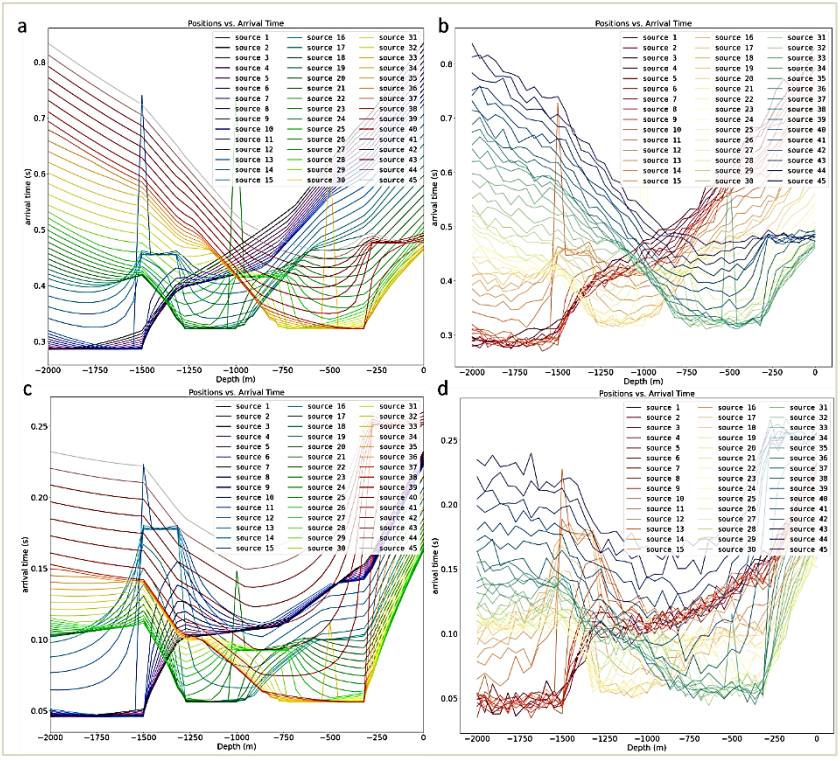

Fig.3 First arrival times of cross-well tomography data for a synthetic multi-layered shale gas reservoir prior to CO2 injection, (a) seismic observed data, (b) seismic predicted data (c) electromagnetic observed data, and (d) electromagnetic predicted data.

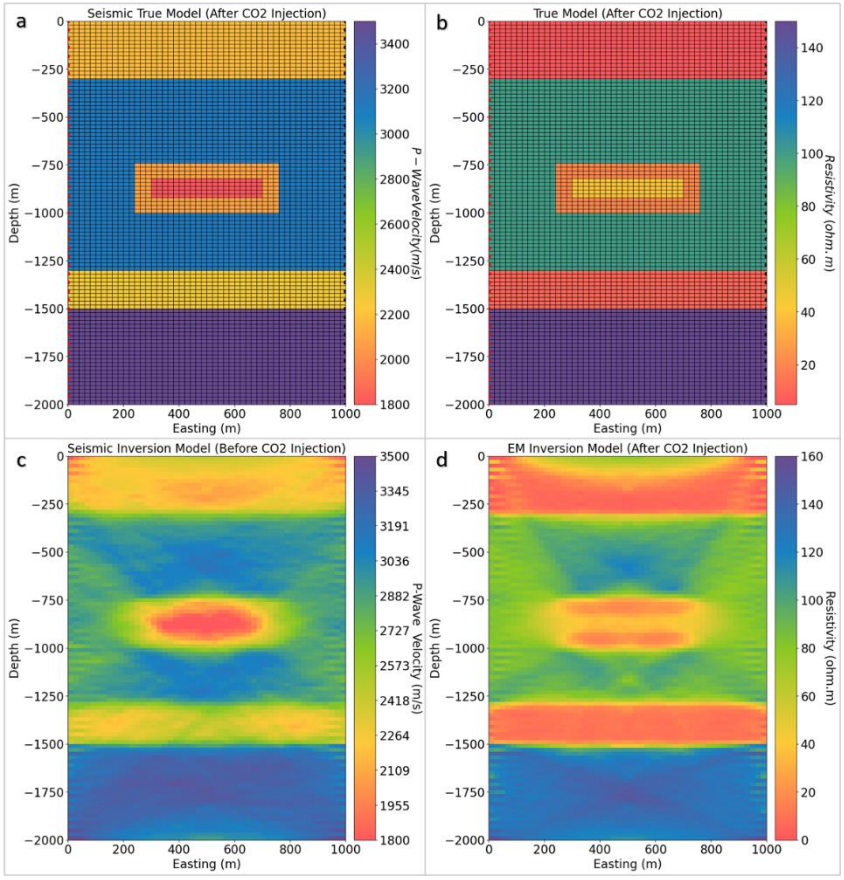

Fig.4 Geophysical simulation of a synthetic multi-layered shale gas reservoir after CO2 injection, focusing on two physical properties: (a) the P-wave velocity model, and (b) the electrical resistivity model. The mixed-norm inversion technique was applied to cross-well tomography data, resulting in (c) the P-wave velocity model and (d) the electrical resistivity model.

For this reason, it is essential to set misfit targets relative to the noise (e.g. reduced $\chi 2 \approx 1$), monitor model change per IRLS step, and use IRLS stopping controls (misfit tolerance, $f_{\min\ \_change}$) to avoid over- or under-fitting. Detectability also depends strongly on the inversion hyperparameters. The smallness/gradient norms control the character of the solution: $p \approx 2$ yields smooth, robust but blurred models; $p \approx 1$ produces sharper, more compact anomalies; $p \to 0$ gives very sparse, high-contrast blocks but at the cost of non-convexity and sensitivity to initialization and noise. Practical choices are therefore a trade-off (e.g. moderate p, smaller q for sharper edges when SNR allows). Numerical controls matter too: the IRLS threshold ε stabilizes weight updates (too small leads to ill-conditioning; too large leads to suppressed sparsity), cooling must be gradual to avoid local minima, β balances fit versus regularity (large β reduces detectability, small β risks overfitting), and regularization multipliers, bounds, and solver tolerances all influence amplitude recovery, depth bias and convergence.

Our base model accurately captured the P-wave velocity and electrical resistivity distributions across the different layers. The first layer maintained its predefined characteristics, with an estimated P-wave velocity of approximately 2,100 m/s and an electrical resistivity of 5 Ω·m. Similarly, the second layer was successfully reconstructed with a P-wave velocity of about 3,100 m/s and a resistivity close to 100 Ω·m. The third layer's physical properties were recovered as a P-wave velocity of 2,200 m/s and a resistivity of 10 Ω·m, while the final limestone layer exhibited a P-wave velocity of 3,500 m/s and an electrical resistivity of 150 Ω·m.

Crucially, the inversion process effectively identified the target reservoir within the second layer, revealing its P-wave velocity and resistivity before injection as approximately 2,000 m/s and 20 Ω·m, respectively. This result aligns well with our synthetic model. Furthermore, the inversion successfully delineated the target block's position with high accuracy. The reliability of these results was confirmed by the root mean square (RMS) values of 1.27 for the P-wave velocity model and 1.36 for the electrical resistivity model, indicating a high-quality inversion.

The inversion process utilized a discretized squared mesh of 100 × 50 cells, each with a 20 × 20 m dimension, identical to the forward modeling mesh. This mesh was sufficiently dense for the analysis. Figure 3 presents the first arrival diagrams of P-wave velocity and the square root of diffusivity before CO_2 injection. Figure 3a shows the P-wave travel-time between each source and receiver for both observed and predicted data, while Figure 3b depicts the travel-time of the diffusivity factor for both observed and predicted data.

Figure 4 illustrates the scenario following the injection of CO_2 into our target block. As shown, we introduced a block into the target zone, with a width of 400 meters, a height of 100 meters, a P-wave velocity of 1,700 m/s, and an electrical resistivity of 40 Ω·m. These parameters represent the physical variations induced by the injection of CO_2 gas into the zone. The primary objective is to capture the variations in the target block using the mixed-norm inversion of travel-time data between the source and receiver points.

Upon examining Figures 4c and 4d, it is evident that we successfully traced the changes in P-wave velocity and electrical resistivity using the mixed-norm inversion algorithm, with root mean square (RMS) values of 1.32 and 1.39, respectively. A comparison between Figures 3c and 4c reveals a reduction of nearly 300 m/s in the P-wave velocity within the middle section of the target block. Similarly, comparing Figures 3d and 4d shows a clear increase of 20 Ω·m in the electrical resistivity of the middle zone of the block. These results demonstrate that we have accurately captured both the variation and location of the physical properties, confirming that our monitoring system is effective in tracking changes within the structure.

Figure 5 presents the travel-time graphs for the observed and predicted models. To further investigate the time-lapse variation of P-wave velocity and electrical resistivity, Figure 6 illustrates the differences between the inverse models of the seismic and EM data before and after CO_2 injection.

As shown, the differences in the inversion results for the target block, in terms of P-wave velocity and electrical resistivity, are presented in Figures 6c and 6d, respectively. The significant variations in these physical properties at the center of the target block are clearly evident, with the P-wave velocity decreasing by nearly 300 m/s and the electrical resistivity increasing by 20 Ω·m. Another time-lapse representation of the shale gas reservoir is provided in Figure 7.

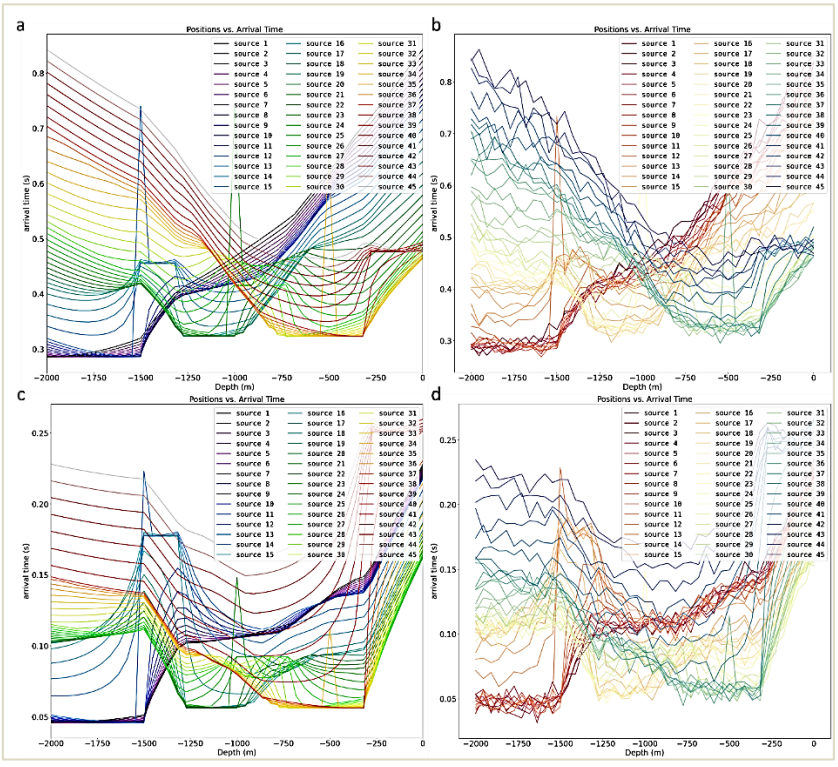

Fig.5 First arrival times of cross well tomography data for a synthetic multi-layered shale gas reservoir after CO2 injection, (a) seismic observed data, (b) seismic predicted data (c) electromagnetic observed data, and (d) electromagnetic predicted data.

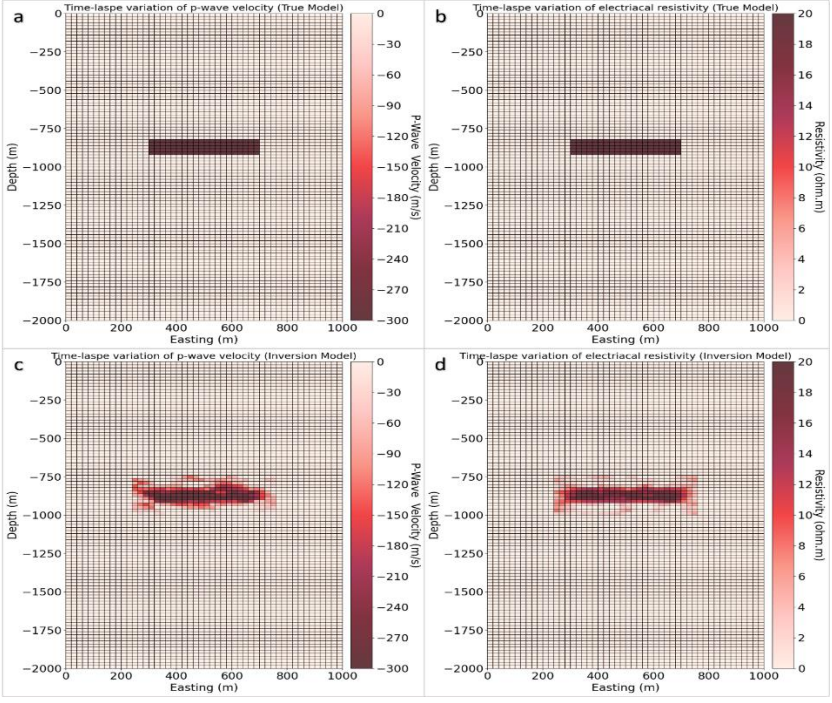

Fig.6 Time lapse variation of physical characteristics of the synthetic multi-layered shale gas reservoir after CO2 injection, (a) the P-wave velocity model, and (b) the electrical resistivity model. The variation of inversion results has been shown for (c) P-wave velocity model, and (d) electrical resistivity model.

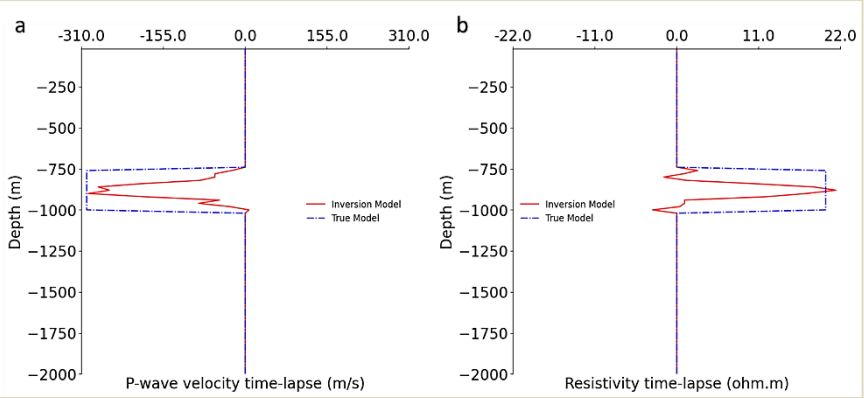

Fig.7 Time lapse variation of physical characteristics along a well at the center of synthetic multi-layered shale gas reservoir, (a) P-wave velocity model, and (b) electrical resistivity model. Assumed and predicted physical variation curves have been plotted.

As demonstrated, this diagram illustrates the time-lapse variation of both P-wave velocity and electrical resistivity at the center of the synthetic multilayer model along the boreholes (depth). As shown, the time-lapse variation of P-wave velocity at a specific depth level (the middle of the target block) is a decrease of 300 m/s, as expected. Additionally, the time-lapse variation in resistivity of the synthetic model is 20 Ω·m. These time-lapse variations clearly highlight the physical changes in the target zone, both before and after the CO_2 injection process, making the discrepancies in physical properties traceable.

Extending our workflow from 2D to 3D cross-hole seismic–EM tomography would provide more realistic plume imaging by capturing the full spatial complexity of CO_2 migration, including lateral heterogeneities and out-of-plane flow pathways that cannot be fully resolved in 2D sections. The primary benefit of 3D monitoring lies in improved accuracy of plume delineation and leakage detection, which has been demonstrated in both field studies and synthetic tests of CO_2 storage monitoring [36,46,51]. However, 3D inversion significantly increases computational demands due to the larger model parameter space and denser acquisition geometries, requiring high-performance computing resources and efficient regularization strategies. Despite these challenges, advances in 3D time-lapse seismic and resistivity imaging show that such extensions are feasible and yield higher-fidelity reservoir characterizations, thereby enhancing the reliability of long-term CO_2 monitoring.

5. Conclusions

Time-lapse monitoring of CO_2 reservoirs is crucial for detecting the presence and variation of CO_2 within geological structures. The 4D time-lapse monitoring approach relies on the discrepancies in the measured physical properties of the target zone, using various geophysical methods before and after the CO_2 injection process. Cross-well tomography is a powerful technique that ensures the success of obtaining high-resolution 2D models. In this study, we employed P-wave velocity tomography through cross-well measurements, which is essential for tracking the movement of injected CO_2 in subsurface reservoirs, as well as for assessing reservoir integrity, caprock sealing efficiency, and potential leakage pathways. Since P-wave velocity is sensitive to fluid saturation and rock stiffness, it can reveal changes in pore fluid composition caused by CO_2 injection. P-wave velocities tend to decrease in CO_2-saturated zones because CO_2 has a lower density and bulk modulus compared to brine. Therefore, we utilized this characteristic to design a synthetic model with decreased P-wave velocity in the target zone, aiming to capture this physical variation through appropriate modeling.

To enhance the accuracy of monitoring CO_2 injections, we incorporated the EM cross-well tomography technique, which enables us to trace changes in electrical resistivity during CO_2 injection. Typically, CO_2 is a poor conductor of electricity compared to brine, so its presence leads to an increase in electrical resistivity within the reservoir. This property was applied to the synthetic geological model. We leveraged the high sensitivity of the EM method to fluid changes, which is more pronounced than seismic approaches, to integrate the results from both seismic and EM tomography. This combination allowed us to obtain reliable results regarding the effect of CO_2 injection on various physical properties.

The integration of suitable geophysical methods with capable inversion algorithms is vital for precise time-lapse monitoring. The effectiveness of the inversion technique is essential for detecting CO_2-saturated zones, even when the physical variations are subtle. Based on the results, the synthetic variations of P-wave velocity (a decrease of 300 m/s) and electrical resistivity (an increase of 20 Ω·m) were successfully captured using the mixed-norm inversion algorithm, which showed expected differences in the measured physical properties. Consequently, cross-well seismic and EM tomography effectively monitored the impact of CO_2 injection into gas shale reservoirs through various geophysical measurements.

Data availability statement

Simulated data are available upon reasonable request to the corresponding author via the email address maysamabedi@ut.ac.ir.

Acknowledgements

We wish to convey our heartfelt gratitude to the School of Mining Engineering and the Institute of Geophysics at the University of Tehran for their unwavering support throughout our endeavors. Additionally, we would like to express our profound appreciation to the members of the UBC GIF for their generous provision of the SimPEG environment, which has been instrumental in our work.

References

[1] Caineng, Z., Zhi, Y., Zhang, G., Lianhua, H., Rukai, Z., Shizhen, T., Xuanjun, Y., Wang, Y., Guo, Q., WANG, L., Haibin, B.I., 2014. Conventional and unconventional petroleum "orderly accumulation": concept and practical significance. Pet Explor Dev. 41(1),14-30.

[2] Muther, T., Qureshi, H.A., Syed, F.I., Aziz, H., Siyal, A., Dahaghi, K., Negahban, S., 2022. Unconventional hydrocarbon resources: geological statistics, petrophysical characterization, and field development strategies. J Petrol Explor Prod Technol. 12, 1463-1488.

[3] Song, Y., Li, Z., Jiang, L., Hong, F., 2015. The concept and the

accumulation characteristics of unconventional hydrocarbon resources. Pet Sci. 12(4), 563-572.

[4] Hamada, G.M., 2016. Comprehensive Evaluation and Development of Unconventional Hydrocarbon Reserves as Energy Resource. Petro and Envi Biotech., APEB-102.

[5] Heikal, S., 2008. Scope of Tight Gas Reservoir in Pakistan. Pakistan Petroleum Exploration & Production Companies Association (PPEPCA), Islamabad, Pakistan.

[6] Huang, T., Xie, B., Ran, Q., Zou, D., Zhong, G., 2015. Geophysical evaluation technology for shale gas reservoir: A case study in Silurian of Changning Area in Sichuan Basin. Energy Exploration & Exploitation 33 (3), 419-438.

[7] Kumar, D., Hoversten, M., 2012. Geophysical model response in a shale gas. 9th Biennial International Conference & Exposition on Petroleum Geophysics. Hyderabad, 1-7.

[8] Nazarenko, M.Y., Kondrasheva, N., Saltykova, S.N., 2018. Electrical Resistivity of Coal and Oil Shales. Coke and Chemistry 61(5), 184-187.

[9] Abedi, M., 2024. 2D Simulation of Shale Gas Reservoir through Z-Axis Tipper Electromagnetic Data. Journal of Petroleum Geomechanics 7 (4), 26-37.

[10] Senger, K., Birchall, T., Betlem, P., Ogata, K., Ohm, S., Olaussen, S., Paulsen, R.S., 2021. Resistivity of reservoir sandstones and organic rich shales on the Barents Shelf: Implications for interpreting CSEM data. Geoscience Frontiers 12 (6), 101063.

[11] Wang, C., Shi, Z., Yang, W., Wei, Y., Huang, M., 2022. High-resolution shallow anomaly characterization using cross-hole P- and S-wave tomography. Journal of Applied Geophysics 201, 104649.

[12] Silver, P. G., Daley, T. M., Niu, F., Majer, E.L., 2007. Active source monitoring of cross-well seismic travel time for stress-induced changes. Bulletin of the Seismological Society of America 97(1B), 281-293.

[13] Gritto, R., Daley, T.M., Myer, L.R., 2002. Joint cross well and single well seismic studies at Lost Hills, California. Geophysical Prospecting 52, LBNL-50651.

[14] Harris, J.M., 1988. Cross-well seismic measurements in sedimentary rocks. In SEG Technical Program Expanded Abstracts 1988 (pp. 147-150). Society of Exploration Geophysicists.

[15] Tucker, K. E., Harris, P. M., Nolen-Hoeksema, R.C., 1998. Geologic investigation of cross-well seismic response in a carbonate reservoir, McElroy field, west Texas. AAPG bulletin 82(8), 1463-1503.

[16] Cao, S., Greenhalgh, S., 1997. Cross-well seismic tomographic delineation of mineralization in a hard-rock environment. Geophysical Prospecting 45(3), 449-460.

[17] Becht, A., Bürger, C., Kostic, B., Appel, E., Dietrich, P., 2007. High-resolution aquifer characterization using seismic cross-hole tomography: An evaluation experiment in a gravel delta. Journal of Hydrology 336(1-2), 171-185.

[18] Zhdanov, M.S., 2009. Geophysical electromagnetic theory and methods (Vol. 43). Elsevier.

[19] Munoz, G., 2014. Exploring for geothermal resources with electromagnetic methods. Surveys in geophysics 35, 101-122.

[20] Ghanbarifar, S., Ghiasi, S. M., Hosseini, S. H., Abedi, M., Oskooi, B., Smirnov, M.Y., 2024. Geoelectrical image of the Sabalan geothermal reservoir from magnetotelluric studies. Journal of Applied Geophysics 224, 105359.

[21] Hosseini, S.H., Oskooi, B., Ghanbarifar, S., Ghiasi, S. M., Abedi, M., Smirnov, M.Y., 2024. 2D sharp boundary inversion to determine tectonic and geological features of geothermal fields through the magnetotelluric method: case study of the Mahallat reservoir in Iran. Bulletin of Geophysics and Oceanography 65 (3), 347-376.

[22] Wilt, M. J., Alumbaugh, D. L., Morrison, H. F., Becker, A., Lee, K. H., Deszcz-Pan, M., 1995. Crosswell electromagnetic tomography: System design considerations and field results. Geophysics 60(3), 871-885.

[23] Zhdanov, M.S., Yoshioka, K., 2003. Cross-well electromagnetic imaging in three dimensions. Exploration Geophysics 34(2), 34-40.

[24] Torres-Verdin, C., Habashy, T.M., 1993. Cross-well electromagnetic tomography. In 3rd International Congress of the Brazilian Geophysical Society (pp. cp-324). European Association of Geoscientists & Engineers.

[25] Nekut, A.G., 1995. Crosswell electromagnetic tomography in steel-cased wells. Geophysics 60(3), 912-920.

[26] Marsala, A. F., AlRuwaili, S., Ma, S. M., Modiu, S. L., Ali, Z., Donadille, J. M., Wilt, M., 2007. Crosswell electromagnetic tomography in Haradh field: modeling to measurements. In SPE Annual Technical Conference and Exhibition? (pp. SPE-110528). SPE.

[27] Alumbaugh, D.L., Morrison, H.F., 1995. Monitoring subsurface changes over time with cross-well electromagnetic tomographyt1. Geophysical Prospecting 43(7), 873-902.

[28] Böhm, G., Brauchler, R., Nieto, D., Soncin, G., Baradello, L., Pivetta, M., Botti, F., 2011. Experimental correlations between geophysical and hydraulic parameters from different inversion procedures. In Near Surface 2011-17th EAGE European Meeting of Environmental and Engineering Geophysics (pp. cp-253). European Association of Geoscientists & Engineers.

[29] Carcione, J.M., Gei, D., Picotti, S., Michelini, A., 2012. Cross-hole electromagnetic and seismic modeling for CO2 detection and monitoring in a saline aquifer. Journal of Petroleum Science and Engineering 100, 162-172.

[30] Simakov, A., Vakulenko, S., Politcina, A., Ivanov, P., Rusakov, E., Marchenko, M., Shustov, N., 2020. Efficiency Evaluation of High-Resolution Seismic; Electrical Resistivity Tomography and Electromagnetic Surveys on Rivers, Based on Modelling Studies. In Engineering and Mining Geophysics 2020 (Vol. 2020, No. 1, pp. 1-12). European Association of Geoscientists & Engineers.

[31] Warren, I., Gasperikova, E., Pullammanappallil, S., Grealy, M., 2018. Mapping geothermal permeability using passive seismic emission tomography constrained by cooperative inversion of active seismic and electromagnetic data. In Proceedings of the 43rd Stanford Workshop on Geothermal Reservoir Engineering, Stanford, CA, USA (pp. 12-14).

[32] Jia, B., Tsau, J. S., Barati, R., 2019. A review of the current progress of CO2 injection EOR and carbon storage in shale oil reservoirs. Fuel 236, 404-427.

[33] Janna, F., Le-Hussain, F., 2020. Effectiveness of modified CO2 injection at improving oil recovery and CO2 storage—Review and simulations. Energy Reports 6, 1922-1941.

[34] Abedini, A., Torabi, F., 2014. On the CO_2 storage potential of cyclic CO_2 injection process for enhanced oil recovery. Fuel 124, 14-27.

[35] Iddphonce, R., Wang, J., Zhao, L., 2020. Review of CO2 injection techniques for enhanced shale gas recovery: Prospect and challenges. Journal of Natural Gas Science and Engineering 77, 103240.

[36] Arts, R., Eiken, O., Chadwick, A., Zweigel, P., Van der Meer, L., Zinszner, B., 2004. Monitoring of CO2 injected at Sleipner using time-lapse seismic data. Energy 29(9-10), 1383-1392.

[37] Mito, S., Xue, Z., Ohsumi, T., 2008. Case study of geochemical reactions at the Nagaoka CO2 injection site, Japan. International journal of greenhouse gas control, 2(3), 309-318.

[38] Michelini, A., 1995. An adaptive-grid formalism for traveltime tomography. Geophysical Journal International 121(2), 489-510.

[39] Carcione, J.M., 2007. Wave fields in real media: Wave propagation in anisotropic, anelastic, porous and electromagnetic media. Elsevier.

[40] Carslaw, H.S., 1959. J. c. Jaeger. Conduction of heat in solids, 2.

[41] Oristaglio, M.L., Hohmann, G.W., 1984. Diffusion of electromagnetic fields into a two-dimensional earth: A finite-difference approach. Geophysics 49(7), 870-894.

[42] Tikhonov, A.N., & Arsenin, V.Y., 1977. Solutions of ill-posed problems. VH Winston & Sons.

[43] Li, Y., Oldenburg, D.W., 1996. 3-D inversion of magnetic data. Geophysics 61(2), 394-408.

[44] Li, Y., Oldenburg, D.W., 1998. 3-D inversion of gravity data. Geophysics, 63(1), 109-119.

[45] Fournier, D., Oldenburg, D.W., 2019. Inversion using spatially variable mixed ℓ p norms. Geophysical Journal International 218(1), 268-282.

[46] Bergmann, P., Schmidt-Hattenberger, C., Labitzke, T., Wagner, F. M., Flechsig, C., Rippe, D., & Ivanova, A. 2012. Surface-downhole electrical resistivity tomography applied to monitoring of CO_2 storage at Ketzin, Germany. Geophysics, 77(6), B253–B267. https://doi.org/10.1190/geo2011-0515.1

[47] Lebedev, M., Pervukhina, M., Mikhaltsevitch, V., Dance, T., Bilenko, O., & Gurevich, B. 2013. An experimental study of acoustic responses on the injection of supercritical CO_2 into sandstones from the Otway Basin. Geophysics, 78(5), D393–D402 (article numbering varies by publisher site). https://doi.org/10.1190/geo2012-0528.1

[48] Mikhaltsevitch, V., Lebedev, M., & Gurevich, B. 2014. A laboratory study of the elastic and anelastic properties of sandstone flooded with supercritical CO_2 at seismic frequencies. Energy Procedia, 63, 3055–3062. https://doi.org/10.1016/j.egypro.2014.11.329

[49] NETL (National Energy Technology Laboratory). 2012. Monitoring, Verification, and Accounting (MVA) for geologic storage projects – Best Practices Manual (DOE/NETL-2012/1568). U.S. Department of Energy. (Reports Ketzin crosswell ERT increases up to ~200% over baseline.) https://netl.doe.gov/sites/default/files/2018-10/BPM-MVA-2012.pdf

[50] Schmidt-Hattenberger, C., Bergmann, P., Labitzke, T., & Wagner, F. M. 2014. CO_2 migration monitoring by means of electrical resistivity tomography (ERT): Review on five years of operation of a permanent ERT system at the Ketzin pilot site. Energy Procedia, 63, 4366–4373. https://doi.org/10.1016/j.egypro.2014.11.471

[51] Schmidt-Hattenberger, C., Bergmann, P., Labitzke, T., Wagner, F. M., Just, A., Flechsig, C., & Rippe, D. 2016. Permanent crosshole electrical resistivity tomography (ERT) as an established method for the long-term CO_2 monitoring at the Ketzin pilot site. International Journal of Greenhouse Gas Control, 52, 432–448. https://doi.org/10.1016/j.ijggc.2016.07.021

[52] Shi, J.-Q., Xue, Z., & Durucan, S. 2007. Seismic monitoring and modelling of supercritical CO_2 injection into a water-saturated sandstone: Interpretation of P-wave velocity data. International Journal of Greenhouse Gas Control, 1(4), 473–480. https://doi.org/10.1016/j.ijggc.2007.07.002

[53] Spetzler, J., Zelt, C. A., Xue, Z., & Würdemann, H. 2008. Time-lapse crosswell seismic tomography for monitoring CO_2 storage at Nagaoka, Japan. Geophysical Journal International, 172(1), 214–225. https://doi.org/10.1111/j.1365-246X.2007.03615.x

[54] Falcon-Suarez, I., North, L., Amalokwu, K., Delgado-Martin, J., Callow, B., Robert, K., & Sahoo, S. K. 2020. Electrical resistivity of Fontainebleau sandstone as a function of brine saturation: A comparative study. International Journal of Greenhouse Gas Control, 100, 103114. https://doi.org/10.1016/j.ijggc.2020.103114